Research Paper

Experimental COP optimization procedure in an air-based reverse Brayton cycle for cryogenic applications

J.R. Serrano, L.M. García-Cuevas, A. Gómez-Vilanova *, J.A. López-Carrillo

CMT – Clean Mobility and Thermofluids, Universitat Politècnica de València Camino de Vera, 46022 Valencia, Spain

A B S T R A C T

Sustainable and efficient refrigerants are essential due to increasing regulatory constraints on traditional high-GWP refrigerants. This study investigates the potential of natural refrigerants, specifically air, in Reverse Brayton Cycles (RBC) for low-temperature applications. Unlike carbon dioxide and ammonia, which pose limitations and safety concerns below −40 °C, air offers a safer and more versatile solution due to its excellent thermodynamic properties and availability. An experimental RBC was constructed using automotive components like centrifugal compressors, a radial turbine, and inter-coolers. These cost-effective and accessible components shift the refrigeration paradigm. The RBC was tested to optimize the Coefficient of Performance (COP) at −100 °C while dissipating 2 kW, a typical scenario for whole-body cryotherapy (WBC). Key control parameters included the pressure ratio of the centrifugal compressors and the position of the stator vanes in the variable geometry turbine (VGT). The optimization process resulted in a COP increase of up to 28 %. Additionally, a 1D gas-dynamic model validated these results, suggesting that different component selections could enhance performance by 17 % compared to the experimental optimum point. Air-based RBC systems using automotive components can effectively achieve temperatures below −40 °C, offering a viable, eco-friendly alternative to traditional refrigerants. This advancement addresses regulatory challenges and contributes to the scientific community by providing a sustainable refrigeration solution using commercially available components and demonstrating improvements through experimental data.

1. Introduction

The sought for alternatives in refrigeration technologies has been a constant concern since the first generation of refrigerant fluids came up during the *XIX*th century. According to J.M. Calm [1], four generations of refrigerants are distinguished. From 1830 to 1930, the first period is defined as "whatever worked" and gases were either flammable, toxic, reactive, or a combination of them [2]. Looking for safety and durability, a second generation of refrigerant fluids came up during the decade of 1930s [3]. Fluorochemicals led then the market for more than 50 years. Chlorofluorocarbons (CFCs) and hydrochlorofluorocarbons (HCFCs) allowed the spread of refrigeration technologies worldwide, contributing to industrial applications, thermal comfort as air conditioners and heat pumps, and preserving products, such as food, drugs, and vaccines. However, the CFCs had a huge ozone depletion potential (ODP), which caused great concern and provoked the international treaty of the Montreal Protocol, first signed in 1987 with subsequent amendments [4] to be specifically designed to protect the ozone layer. A progressive phase-out of almost every

CFC refrigerant fluid was established for the ongoing decades, bringing the third generation of refrigerants from the decade of 1990s, which focused on ozone layer protection. A notably successful effect was noted regarding ozone depletion, as reported by the World Meteorological Organization [5], contrasting with a worsening climate change situation and the global average air and ocean temperatures increase during the 2000s [6,7]. The high global warming potential (GWP) level of most fluorochemicals (F-gases) came up with the 4th generation of refrigerants from 2010 in advance, where low-GWP refrigerant fluids should help mitigate global warming [8].

Under the exposed situation, using natural refrigerants is an attractive solution to meet the requirements of this fourth generation of refrigerants [9]. Ammonia, carbon dioxide, water, hydrocarbons, and air have null ODP, zero or very low GWP compared with fluorochemicals, and their safety and availability, despite being variable among them, are usually higher and more economical than F-gases.

Ammonia (R-717) is a widely used refrigerant for medium and large-scale refrigeration systems. Both GWP and ODP values equal 0

* Corresponding author.
E-mail addresses: jrserran@mot.upv.es (J.R. Serrano), luiga12@mot.upv.es (L.M. García-Cuevas), algovi2@mot.upv.es (A. Gómez-Vilanova), jualoca6@mot.upv.es (J.A. López-Carrillo).

Nomenclature

Symbols and acronyms

A	Heat transfer exchange area [m^2]
α_{VGT}	Angle of turbine stator vanes
CAPEX	Capital expenditures
CC	Climatic Chamber
CCyc	Closed cycle
CFC	Chlorofluorocarbon
COP	Coefficient of Performance [-]
c_p	Specific Heat at Constant Pressure [J/kg/K]
EC	Electric Compressor
GHG	Greenhouse gases
GWP	Global Warming Potential
γ	Specific heat ratio
η	Corresponding Efficiency [%]
HCFC	Hydrochlorofluorocarbon
IC	Inter-Cooler
LMTD	Logarithmic Mean Temperature Difference
$\dot{m}$	Mass Flow Rate [kg/s]
MFR	Mass Flow Rate [kg/s]
n	Rotational speed [rpm]
OC	Open cycle
ODP	Ozone Depletion Potential
OPEX	Operational expenditures
p	Pressure [bar]
π	Pressure ratio
Q	Exchanged heat in an intercooler [W]
$\dot{Q}$	Heat flow [W]
Q_w	Water flow rate [kg/s]
RBC	Reverse Brayton Cycle
Re	Reynolds number [-]
REC	Recuperator
SF	Scaling Factor of the turbine
T	Temperature [K]
TCC	Turbocharger Compressor
ThC	Thermocouple
Turb	Turbine
U	Heat transfer coefficient [W/m^2/K]
VEMOD	Virtual Engine Model
VGT	Variable Geometry Turbine
$\dot{W}$	Work
WBC	Whole-Body Cryotherapy
Ω	Nondimensional turbine speed

Subscripts and superscripts

0	Total conditions
a	Air
CC	Climatic Chamber
comp	Compressor
EC	Electric Compressor
IC	Inter-Cooler
in	Inlet side
out	Outlet side
RBC	Reverse Brayton Cycle
Rec	Recuperator
TCC	Turbocharger Compressor
TL	Thermal load
Turb	Turbine
w	Water
*	Corrected quantity

for this gas. However, its toxic and flammable properties demand strict safety protocols, often using indirect systems in various applications. Despite these risks, its pungent odor is an early warning system for potential leaks. Its miscibility with water makes water cleaning systems effective for containment. The ignition temperature of ammonia is 651 °C, being then classified as moderately flammable since it requires a robust ignition source. While its production cost and availability are way better than synthetic refrigerants (being a byproduct of the Nitrogen cycle), its corrosive tendency when combined with water is a notable disadvantage, particularly for copper alloys commonly used in refrigeration systems, thus increasing maintenance costs compared to systems employing other refrigerants. Its applications can be found in both vapor compression systems [10] and absorption systems [11]. The boiling point of ammonia is −33 °C, and its melting point is −77.7 °C, limiting the range of actuation, especially for vapor compression systems.

Carbon dioxide (R-744) has zero ODP and a GWP of 1 since it is the reference gas for the index. It is a non-flammable fluid, and while being non-toxic, it can displace the oxygen concentration in breathing air, leading to suffocation and requiring room indicator sensors. It is considered economical compared with F-gases since it can be obtained as a waste product. These refrigerant systems require high working pressures, ranging from hundreds of bar. However, this high pressure, together with the low molar mass of the CO_2 particle, reduces the volumetric flow, thus the facility dimensions. It is employed in food plants [12], marine installations [13]. The use of CO_2 as refrigerant can cover processes up to −40 °C [14], allowing lower temperatures than ammonia, but again is limited to the range above those −40 °C.

Water (R-718), by its part, used as a refrigerant for high-temperature applications (because of its freezing point at 0 °C) is a safe option. It has no dangerous properties such as flammability, toxicity, or explosion hazard. Besides, it has null ODP and <1 GWP, and it is free of future restrictions from laws becoming more strict. The cost is one of the lowest since tap water can be used for refrigerant purposes. Any facility using water as the refrigerant fluid has great operation safety, and pressure ratios are not so high (mainly between 1–10 [15]). The application of water as a refrigerant is done through vapor compression systems, with geometries of the compressor going from centrifugal [16] to screw [17], roots [18] or axial water vapor compressors [19]. However, the range of cryogenic refrigeration is inaccessible for these systems.

Hydrocarbons (HC) such as propane (R-290), propylene (R-1270) or butane (R-600) have been used as refrigerants especially in the petrochemical industry, such as refineries, due to their flammability and explosion limits since those industries are adapted to the treat of flammable fluids [20,21]. According to International Standard IEC 60335 and European Standards EN-378, if HC refrigerant is charged below 150 g, it can be used safely in closed cooling systems without additional safety precautions [22], but measures have to be taken over that quantity of refrigerant, limiting the application to small-sized facilities in several fields. Some authors, such as Giménez-Prades et al. [23], pointed out its low GWP value as a promising alternative for conventional refrigerants mixing R-290 with other fluids to reduce flammability.

Air (R-729) is the safest and cheapest refrigerant from the above-mentioned options. Among its properties, there can be listed null ODP and GWP, minimizing as far as it can be the emissions to the atmosphere; plenty availability, ambient air is entirely viable to be used in any refrigerant cycle, being only necessary to deal with its humidity, and, if necessary pollutant filters; highest safety standards accomplished, non-flammable, non-toxic, and of course, breathable. Again, as it was noted with the water case, there is no reason to ban the use of air as a refrigerant in any case with future regulations. Any facility using air would only be out of phase because of its components if there are better options in the market, but not for the fluid itself (as it happens with other refrigerant fluids having life expectancies between 10 and 20 years [24]). Besides, the operation of air cycles is highly safe, pressure ratios are small (mainly in the range 1–5), any leak is repairable, and would only affect efficiency in what are considered as indirect emissions [25]. Compared with ammonia and

carbon dioxide, the freezing temperature of the air is much lower (−194 °C), and much lower temperatures can be achieved, covering the range of temperatures below −40 °C and reaching temperatures below −100 °C without any problem. This feature converts air systems into a viable alternative, especially for that ultra-low temperature range of application. There is no consensus about which can be the alternative for F-gases at those temperatures for purposes such as vaccines and other heat-sensitive health products [26] since current extended options are HFCs as Fluoroform (R-23) with a GWP value of 12400 or hydrocarbons as ethane (R-170) with an A3 ASHRAE classification [27]. Air systems seem well suited to accomplish both A1 ASHRAE and low-GWP. Also, air-based cycles could then cover other liquefaction tasks as shown in the works by Capra et al. and Jin et al. [28,29].

Its greatest disadvantage is the reduction in COP compared with F-gases, but the absence of taxes and no restrictions on future use turn this type of cycle into a matter of study where different applications have been studied as refrigerated transport [30,31], food freezing [32], cleaning and preserving vehicles, structures, or cultural heritage [33], heat pumps [34], aircraft cabin conditioning [35], or whole-body cryotherapy [36], with the advantage of avoiding anoxia cases due to direct injection of vaporized nitrogen gas [37]. To deal with the COP limitations, the study of the exergy destruction ratio reveals that the increase in efficiency of certain components (mainly the expander [38] and the compressor [39]) is vital to raising COP to its technological limits, making then air-cycles competitive with other alternatives. Using turboexpanders and compressors presents coupling problems that have been addressed in the literature for open-loop RBCs [40] and regenerative RBCs [41], proposing optimization methods for this kind of cycles [42]. Other studies as [43] showed an experimental cascade refrigeration system able to work between −100 °C and −170 °C that showed a COP of 0.127 for −100 °C. [27] presented a Linde–Hampson refrigerator system trying blends of low-GWP refrigerants to replace R23 for applications below −40 °C, but a COP below 0.1 was shown for all the studied range of temperatures. Using blends of different refrigerants with R23, [44] obtained a COP of around 0.6 for a minimum temperature of −85 °C with a cascade system. Another RBC using a turboexpander [45] has recently shown an analysis for temperatures between −55 °C and −135 °C with a maximum cooling capacity of 400 W when the temperature is −100 °C and offering COP values in the range of 0.1 for that temperature. This work addresses the optimization of a reverse Brayton cycle (RBC) experimental facility, and a method to optimize COP for a desired objective in temperature and refrigeration capacity is developed and experimentally tested. After that, a thermo and fluid dynamic model of the facility is depicted, showing the validation of each component, and results for the whole cycle are shown. Finally, an analysis of the results obtained and how to further improve the COP of the cycle by choosing more suitable components is done thanks to the development of the gas-dynamic model of the facility.

2. Description of the RBC

The testing facility designed for evaluating the performance of automotive components as a refrigeration cycle is shown in Fig. 1. Its dimension is approximated as $1.6\,m^3$, but this figure is far from being optimized and can be further reduced, even though, in [46], a similar RBC is developed with a similar volume. The present RBC includes several measuring sensors for research purposes that would not participate in a commercially developed facility. To better understand the cycle, a scheme is illustrated in Fig. 2. The system counts with a series of three compression stages, enhancing efficiency compared to having just one compressor doing all the work. Consequently, the turbine regime is not attached to the speed of the main compressors, which are electrically driven compressors (EC) by two e-motors. We then have the first two degrees of freedom for the facility, with the independent control of the speed of each EC. The components are
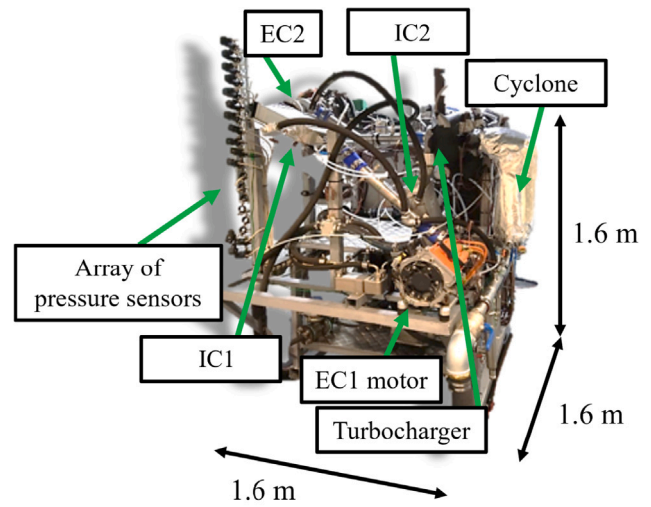

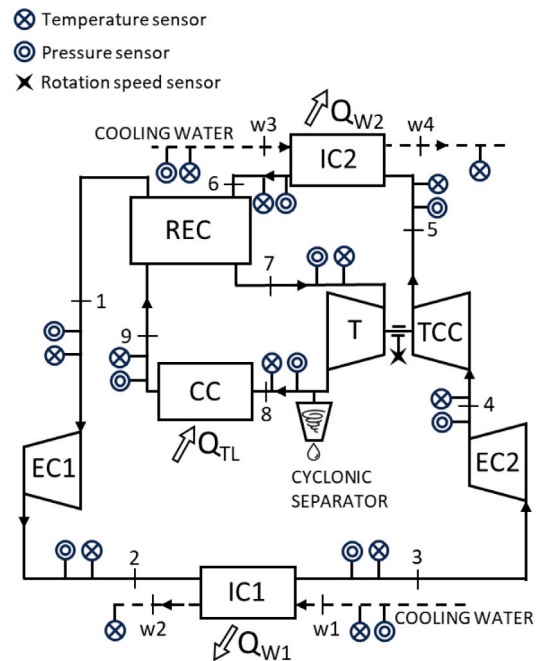**Fig. 1.** Reverse Brayton Cycle test rig.

Fig. 2. Reverse Brayton Cycle diagram.

Rotrex® models EC15-60 and EC15-20 [47]. The turbine power generated in the expansion process (used to cool down the air temperature at every moment) is used in the third compression stage. The main characteristics of the employed turbocharger are shown in Table 1. After the first and the third compressors, there are two water intercoolers, with a double effect of increasing compression efficiency and reducing the temperature at the inlet of the recuperator, which would lead to minimizing the temperature at the turbine inlet.

The RBC developed can actuate both as an open-cycle or closed-cycle system. The closed cycle is performed through a heat exchanger placed on the upper side of the climatic chamber (CC), as shown in Fig. 3. Open-cycle means blowing cold air directly to the climatic chamber versus closed-cycle, that is when air passes through a heat exchanger, which allows different pressures downstream the turbine (Results from closed cycle can be seen in the work by Serrano et al. [41]). The climatic chamber was equipped with several thermocouples evenly
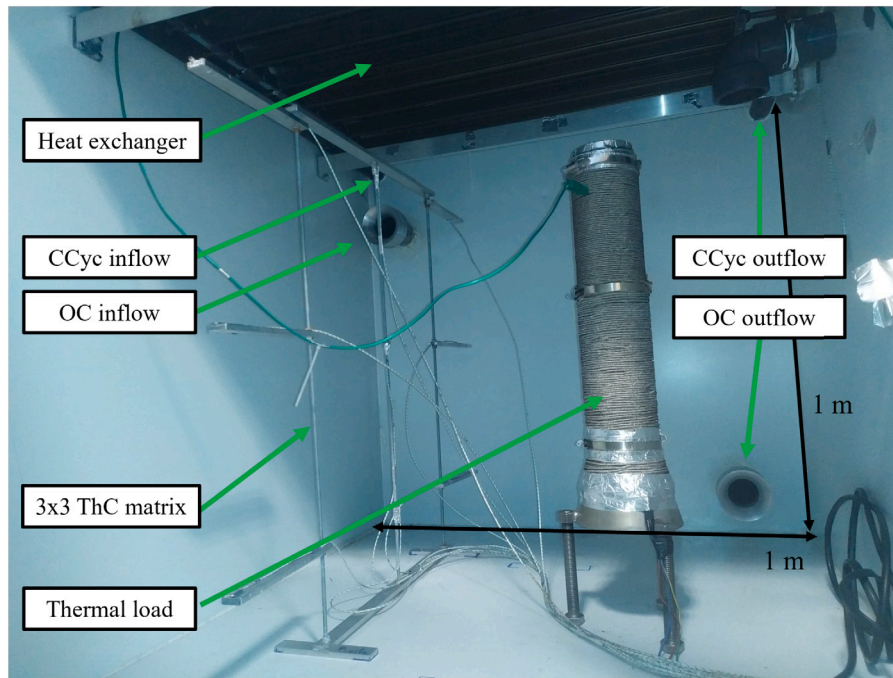
Fig. 3. Climatic chamber used in the RBC facility for temperature measurements.

Table 1
Specifications of the turbocharger.

Turbine	
Wheel diameter	34.5 mm
Stator vane number	11
Rotor blade number	9
Max. reduced mass flow	15 kg s^{-1} K$^{0.5}$ MPa^{-1}
Max. reduced speed	108.3 Hz K$^{0.5}$
Compressor	
Wheel diameter	46.5 mm
Max. corrected mass flow	0.16 kg s^{-1}
Max. corrected speed	170 krpm
Shaft diameter	5.8 mm

distributed to build a map of temperature field distribution inside the cabin, following the work done by António and Afonso [48]. Before entering the climatic chamber, the air passes through a cyclonic separator where condensation droplets are removed from the air stream, removing ice growth in any part of the system and allowing it to work with natural fresh air. Once the climatic chamber is surpassed, the air returns to the recuperator, which will use the low temperature to reduce the turbine inlet temperature, returning then to the inlet of the first compressor. This paper will discuss open-cycle distribution for every studied case. Since the climatic chamber is not designed to stand pressure differences with the ambient, the pressure at the inlet of EC1 will always be closed to ambient conditions (a bit lower because of the pressure drop the system provokes between stages 9–1).

The turbocharger uses oil-fed journal bearings, which, according to different sources [49,50], are not the best choice since they dissipate a significant amount of shaft power due to viscous losses in the oil films (25 % according to Spence et al. [46]), other options as air bearings, magnetic bearings, or high-speed ball bearings became of higher interest. However, the high market availability and low cost of turbochargers equipped with oil-fed bearings make them a suitable choice for a facility that pretends to be cost-effective in terms of CAPEX and not intensive in use to contain OPEX. No change was made to the original components of the turbocharger, nor was there any other

component of the cycle, making it the most accessible prototype to obtain a cryogenic system, thanks to the availability of every component. The turbocharger was tested in a gas stand before its coupling to the RBC [51]. The turbine counts with a variable geometry stator, where the vanes can be placed in different positions, changing the mass flow rate through the facility and adding a third degree of freedom.

The measuring sensors referred to in the previous paragraph are depicted in the scheme of the facility (Fig. 2). Thermocouples and pressure sensors have been placed upstream and downstream of each element in the cycle to assess its performance and gather data for diagnosing and constructing a thermal and fluid dynamic model of the test rig. The features of the transducers employed during the experimental study in the reverse Brayton cycle were:

- Mass flow rate: It is worth noting that although mass flow meters from a turbocharger gas stand were employed to measure turbocharger mass flow rate (MFR), as documented by Serrano et al. [51], they were not directly utilized within the RBC facility. However, the turbomachinery adiabatic maps obtained from the gas stand were representatives for measuring the RBC's mass flow. Measurements described in the aforementioned work [51] were taken at both the inlet and outlet of the turbine and compressor using hot-film and vortex mass flow meters. These were calibrated for air, accommodating a maximum flow rate of $0.200\,\mathrm{kg\,s^{-1}}$. The uncertainty of the device followed a uniform distribution, with a deviation of 1.1 % from the measured value for measurements exceeding $0.005\,\mathrm{kg\,s^{-1}}$, and the disparity between the inlet and outlet was verified. The same actuation took place with the ECs. They were characterized in a gas stand to build performance maps and then used as transducers. Having up to 4 devices to check the MFR (EC1, EC2, TCC, and the turbine) was sufficient to ensure the accuracy of MFR measurement.

- Temperature: Three T-type thermocouples were positioned upstream and downstream of every element. They were radially distributed at the same diameter, separated by 120° between each thermocouple, and inserted to varying depths at 1/2, 1/3, and 1/4 of the pipe diameter. The uncertainty associated with them was 0.5 K. In order to minimize propagated uncertainty, each channel in the acquisition system underwent individual calibration.

- Pressure: Piezoresistive transducers for absolute pressure were utilized at every cycle stage. They were positioned upstream of the thermocouples to prevent measurement distortion. Their measuring range ranged from 0–2.5 bar to 0–6 bar, with an uncertainty exhibiting a non-linearity of 0.5 %.

The uncertainties associated with measured physical quantities, such as temperature or pressure, are carried over when calculating derived parameters like any component efficiency, COP, or refrigeration capacity. In this study, the variability in calculated variables has been assessed through an uncertainty propagation analysis. This uncertainty analysis is crucial for ensuring the acceptability of the precision of derived variables. When the statistical probability distribution of a variable can be assumed, its value can be determined with a confidence level. The methodology employed in this study follows the guidelines outlined by the Joint Committee for Guides and Metrology [52] and has been utilized in previous research endeavors [41,53]. A coverage factor of $k = 2$ has been adopted, implying that, under a normal distribution assumption, the actual values of the derived variable z fall within the range $[z - k \cdot u_z,\ z + k \cdot u_z]$ with a confidence level of 95 %, where u_z represents the uncertainty of the derived variable z. Before the start of the experimental campaign, sensor measurements were cross-checked against calibration instruments to mitigate systematic errors, thus focusing solely on random contributions. The uncertainty (u_z) of a derived quantity z can be determined using Eq. (1). For simplicity, Eq. (1) can be linearized and simplified by incrementally perturbing the mean values with their respective uncertainties:

$$u_z^2 = \sum_{i=1}^{n} \left(\frac{\partial z}{\partial \bar{x}_i} \right)^2 \cdot u_{\bar{x}_i}^2 \approx \sum_{i=1}^{n} \left[z \left(\bar{x}_i + u_{\bar{x}_i} \right) - z \left(\bar{x}_i \right) \right]^2 \tag{1}$$

Where $\bar{x}_1, \bar{x}_2, \ldots \bar{x}_n$ are the mean of the measured quantities.

In previous analyses, the capacity of the cycle has been tested, and up to −145 °C have been achieved in the turbine outlet [41]. Despite covering much of the working capacity of the RBC in those tests, the adequacy of the power needed by each electric compressor for a specific operating point was not evaluated, and there is room for improvement in the COP. For the ongoing analysis, the definition of COP applied will be as shown in Eq. (2)

$$
\begin{aligned}
COP &= \frac{\left(T_{\text{out,CC}} - T_{\text{in,CC}} \right)}{\left(T_{\text{out,EC1}} - T_{\text{in,EC1}} \right) + \left(T_{\text{out,EC2}} - T_{\text{in,EC2}} \right)} \\
&= \frac{\left(T_9 - T_8 \right)}{\left(T_2 - T_1 \right) + \left(T_4 - T_3 \right)}
\end{aligned}
\tag{2}
$$

The COP depends on the efficiency of both electric compressors (ECs). For each operating point, an optimal combination of EC efficiencies results in the highest aerodynamic COP. This analysis excludes electrical losses in the ECs, such as derating or transmission losses.

3. COP optimization procedure

Given the degrees of freedom in the system, an optimal COP is sought. Various speeds will be applied to the electric compressors, and the blade opening in the turbine stator will be utilized. The target point is set to cool 2 kW at −100 °C in the climatic chamber. This working point is a case scenario for whole-body cryotherapy (WBC) [36,54], involving temperatures between −40 °C to −180 °C, while 2 kW could be between one and two people depending on the mass and height of the person. Different electric compressor speeds offer a variability of compression ratios, and with the variable geometry turbine (VGT), control over the mass flow passing through the installation is achieved. Since there are two electric compressors in the facility, three variables come into play: n_1, n_2, and α_{VGT}. Being n_1, and n_2 the rotational speed (expressed as a percentage of the maximum allowable values) in both of the electrically driven compressors and α_{VGT} the position of the VGT stator-blades, varying its value between 0 and 100 (0 for the narrowest possible channel and 100 for fully opened position).
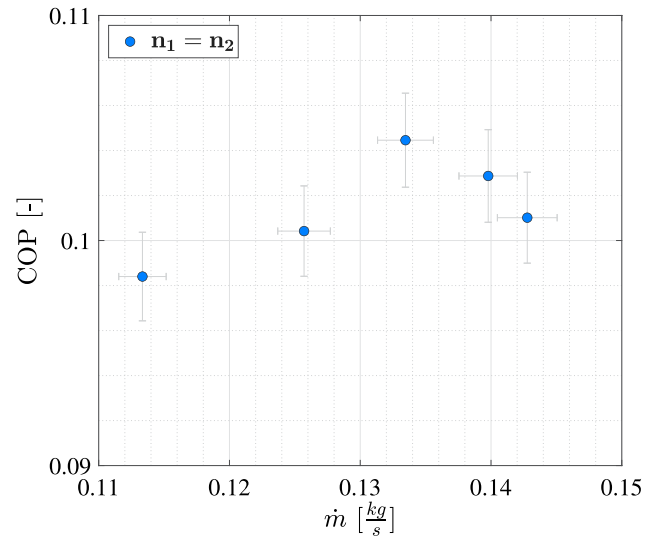

Fig. 4. COP vs MFR for equal speed regimes in both ECs. Experimental results dissipating 2 kW at −100 °C.

The facility counts with an automatic control system that is able to adjust parameters through a proportional–integral–derivative (PID) control to achieve a desired purpose, in this case, the temperature of −100 °C inside the climatic chamber. The parameters that the PID can actuate on are n_1 and n_2. Meanwhile, α_{VGT} has to be manually modified since there is no automatic control on the vane position. Since an experimental optimization process is performed, time matters, and a procedure for the experiment must be established. Based on the work from Spence et al. [46] that showed there is an optimum MFR, alongside a maximum overall pressure ratio (that offers a maximum COP) for a specific operating point (the refrigeration capacity at the desired temperature), a preliminary test is done varying α_{VGT} and adjusting both speed regimes with the PID using the link equation $n_1 = n_2$ (as it was done for every studied point by Serrano et al. [41]). The result of this experiment is shown in Fig. 4, showing a clear trend where a range of mass flow rates optimizes COP. In this case, the optimum MFR is around 0.134 kg s⁻¹, offering a COP of 0.105. For both higher and lower MFRs, achieved varying α_{VGT}, the COP of the system decreases rapidly, lowering by a 5 % at 0.126 kg s⁻¹ and 0.144 kg s⁻¹. There is a trade-off between all the components participating in the cycle to get the desired cooling power. If the MFR is too high, the added work needed from the compressors to move that air mass flow penalizes COP; besides, the optimum efficiency area of the compressor must be considered. The minimum temperature achieved is a function of the turbine efficiency, so α_{VGT} must be placed in a sufficiently good position to ensure the performance of the expansion process.

The two electric compressors are different models. Thus, they do not have the same optimum efficiency ranges of operation. While EC1 offers a wide operating range at its peak (Fig. 7), EC2 shows better behavior at low regime speeds (Fig. 8). According to [38], there are chances of increasing COP with a higher EC2 efficiency. Consequently, an upper bound for n_2 is set at 70 % of its overall capacity, compensating the lack of compression ratio controlling n_1 with a PID. Thus, n_2 and α_{VGT} will be varied independently following the scheme shown in Fig. 5. The goal is to obtain the combination of parameters (n_1, n_2 and α_{VGT}) that offer the maximum COP value. First, a rotational speed below 70 % of n_2 for the second electric compressor is set alongside an α_{VGT} position. Then, α_{VGT} is actuated in one direction, changing the stator vanes position and varying the mass flow through the system until a decrease in COP is noticed. After that, the vanes are moved in the opposite direction (if at first, they were more open each time, now the aim is to close them) to find another change in the trend in COP. That way an optimum α_{VGT}

is found for a certain n_2. From the local optimum point found of α_{VGT} position, a variation of n_2 is done following the same process as done before with α_{VGT}. The repetition of this process drives the convergence of a combination of α_{VGT} and n_2 offering an optimum COP for the established target.

The way the cycle is designed (with no cooling phase between EC2 and TCC) favors a better performance when π_{EC2} is reduced (besides its increase in efficiency because of the compressor map distribution), the temperature at EC2 outlet is lower, and therefore the temperature received by the TCC decreases, minimizing the heat transfer between turbine and compressor in the turbocharger and increasing the pressure ratio in TCC for the same VGT power. In the case of the present RBC, unlike other turbocharger applications, the compressor is much hotter than the turbine, and the higher its temperature, the more affected the cooling capacity of the turbine will be. Thus, by minimizing the outlet temperature of EC2, the RBC has the advantages of a system with series compressions, reducing the need to add an extra cooling stage before TCC. Combining the optimization of π_{EC2} with the variation of α_{VGT}, to place the system at the optimum MFR, will maximize COP. However, this could affect turbine performance since the optimum range in MFR could not match the α_{VGT} that offers the best efficiency for the turbine. This is expected because the turbine was selected from a field different from refrigeration, specifically the automotive industry. The chosen turbine was picked according to the MFR of the electric compressors, trying to fit best with their operating maps. A modeling tool will be used to check the effect of modifying the turbine size.

4. RBC computational model

As it has been explained, the idea of optimizing the cycle might take into account the scale of the turbine and its adequacy with the range of MFR that optimizes COP. It is an element readily available in the market, allowing the exploration of substitutes of different sizes. This is a matter of high interest according to the results from Serrano et al. [38], where it was noticed that for an RBC operating with air, the efficiency of the turbine is the most important parameter when looking for an increase in COP. Hence, with a modeling tool, the turbine size can be scaled up or down while maintaining the performance properties to guess how much enhancement potential there is just by changing the VGT size.

A 1D model of the whole cycle is developed in VEMOD (Virtual Engine Model), a gas-dynamic software created in-house by researchers at CMT-Clean Mobility & Thermofluids, in which its researchers have full control of the physical models implemented in it [55]. The cycle scheme has been built as depicted in Fig. 6. The pipes of the facility were modeled according to the display shown in Fig. 1, being the reason why between EC2 and TCC there is a 3-segment pipe involving two straight ducts with a bent in the middle. The VEMOD scheme of the RBC is separated into three areas: the hot side, involving the two electric compressors and the two intercoolers; the cold side, counting with the climatic chamber, modeled as an intercooler with a heat source applied, and the cyclone, modeled as a straight pipe plus a bent pipe, to simulate the pressure loss provoked; and a third area that is marked as "connection to ambient" that models how a relief valve always keeps the climatic chamber at ambient pressure, with the two reservoirs being infinite deposits of air at ambient conditions. Two PID actuators are connected to the valves to let air flow in or out of the climatic chamber if there are pressure changes in the cycle. Between the hot and cold sides, two components belong to both of them: the turbocharger, with the turbine on the cold side and the compressor on the hot side, and the recuperator, with the points marked as 1, 4 being cold, and the points 2, 3 hot. The operating maps of the two electric compressors were measured in the supplier gas stand. Experimental results have been used to validate these maps, resulting in Figs. 7 and 8. The latter can be used to check how EC2 (Fig. 8) becomes more
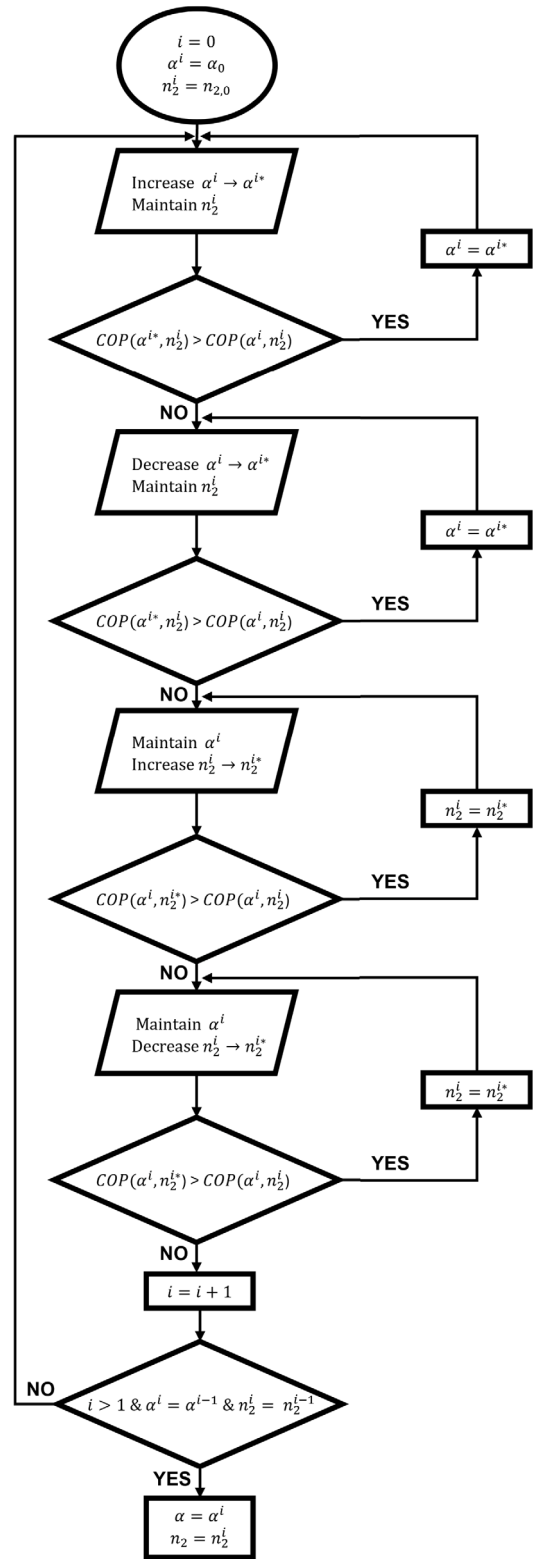

Fig. 5. Flowchart of the proposed optimization technique with COP optimization as objective function, while maintaining a constant dissipated power at a given temperature (2 kW & −100 °C at present study).

interesting with the use of lower EC2 speeds, enhancing compressor efficiency, meanwhile EC1 (Fig. 7) showed a better behavior for medium and high speeds. These figures show the total to total pressure ratio of the compressor π_{comp} against is corrected mass flow MFR^* for a
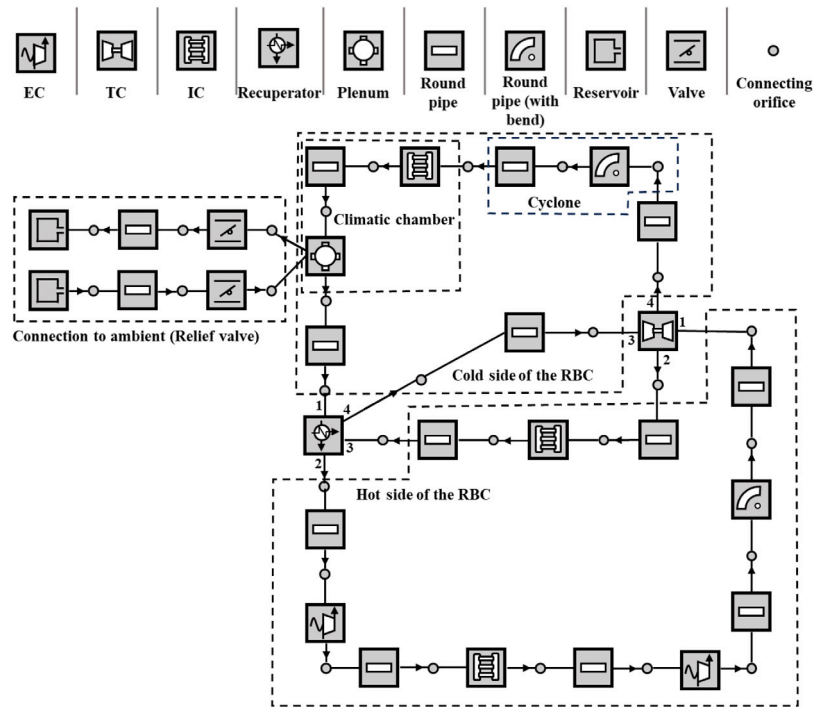
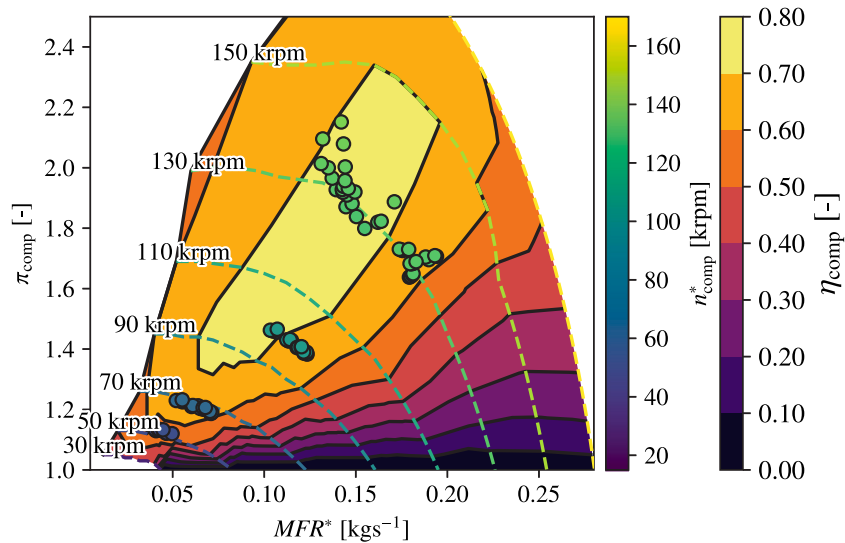**Fig. 6.** Scheme of the thermal and fluid dynamic model of the RBC developed in VEMOD [55].

Fig. 7. EC1 map with experimental points from RBC testing facility.

range of corrected speeds n^*_{comp}, and includes the compressor adiabatic efficiency η_{comp}. Both electric compressors have been experimentally tested trying to cover their whole operating range in terms of mass flow (varying α_{VGT}) and rotational speed (through n_1 and n_2). The model has proved accurate in replicating the experimental response for every covered map area. In this case, there can be seen points following an isospeed line for a range of MFR, that corresponds to constant n_1, n_2 tests, and clouds of dispersed points in the upper side of the map plotted in Fig. 7. That cloud of points is the result of the optimization procedure applied, being those the conjugate points of the sequence of points that cross perpendicularly the 100 krpm speed line plotted in Fig. 8, when searching for the optimum combination of speed regimes, combined with α_{VGT} position, that showed its influence in Fig. 4.

Two different models were applied to the turbocharger. On the one hand, the compressor was modeled as shown in [51], since the same

turbocharger was employed, based on a wide experimental campaign performed on a turbocharger test rig. Experimental results obtained in the RBC through different testing campaigns showed a good agreement with the modeled map of the TCC, according to Fig. 9. It must be considered that the points tested at the RBC facility were not planned to build a whole compressor map by themselves, and that there are different clusters of points corresponding with the different power levels applied to the ECs. That is the reason why the points get together in different areas, but they are not on the same isospeed line. It can be noticed how, despite the wide variation in MFR between different points tested, the pressure ratio of the TCC remains in low values, below 1.25. Corrected speeds obtained in the RBC indicate that the turbocharger is far from being at high speeds, taking into account results from Serrano et al. [51]. Besides, the distribution of experimental points shows how they lie closer to the choke than to the surge area,
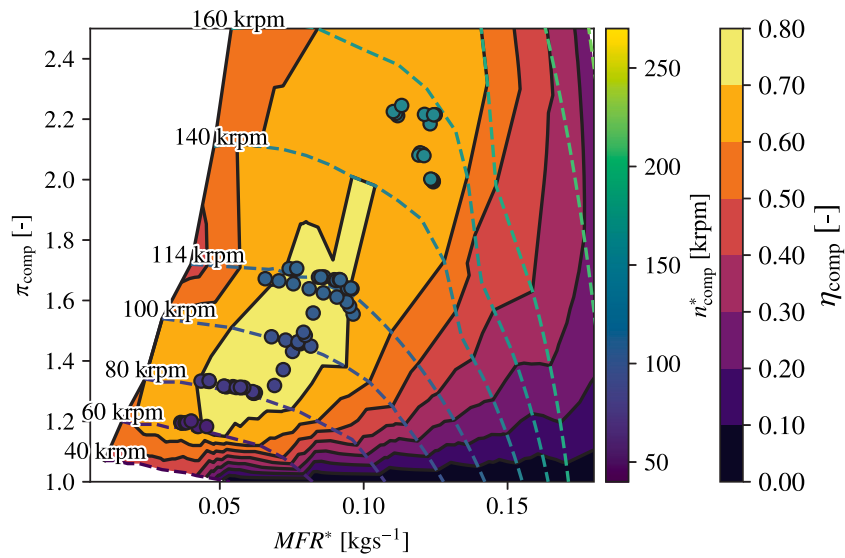
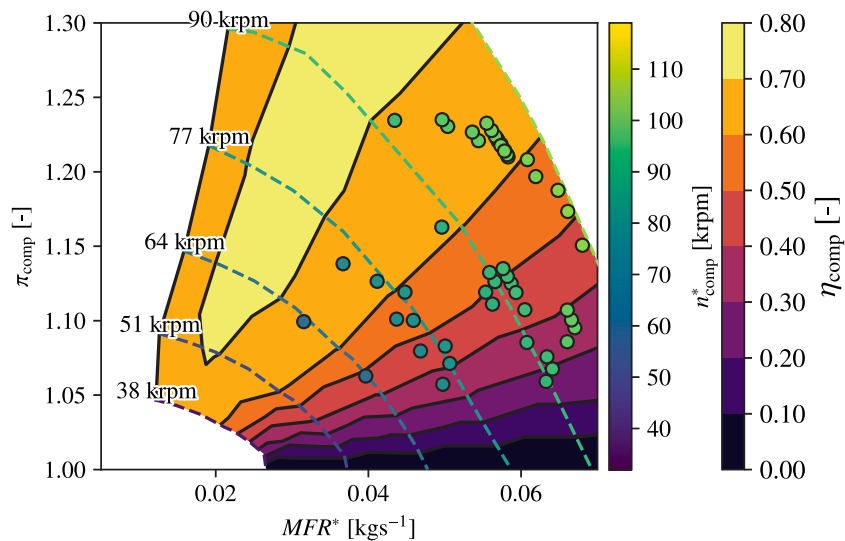**Fig. 8.** EC1 map with experimental points from RBC testing facility.

Fig. 9. TCC map with experimental points from RBC testing facility.

being on the area of the map where the isospeed lines are vertical. With this information, it can be deduced that the TCC size could be increased for the present RBC. That could lead the points to lie in the optimum efficiency area, given that in Fig. 9 none of the points are placed on that area, no matter the workload.

Unlike the compressor, the turbine map measured by Serrano et al. [51] was not useful since the ultra-low temperature conditions in the RBC changed turbine performance compared to the adiabatic measurements, as it was concluded in work done by Serrano et al. in [41], where the extreme cold conditions affected turbine efficiency, having lower peak efficiencies in the RBC facility than in the turbocharger test bench. Therefore, a new turbine map was built and fed with experimental points exclusively obtained in the RBC test bench. The map counted with α_{VGT} positions up to 40 %, being this the widest one tested at the RBC, since the COP of the facility decreased for every test done in positions over that one, indicating that the turbine size would be bigger than needed for the RBC. Thus, through different experimental campaigns involving different target temperatures, from 0 °C to −150 °C, and a range of thermal loads downstream the turbine, various α_{VGT} positions and expansion ratio were tested. As part of the employed dataset, in Fig. 10 there can be seen three α_{VGT} positions,

each of them with three reduced speeds tested. The turbocharger model developed by Serrano et al. [56,57] was used to extrapolate a whole map, obtaining a good accuracy in the obtained model. Peak efficiency points obtained are in the range of 0.6. Meanwhile, according to results from Serrano et al. [51], up to 0.7 was expected for α_{VGT} of 40 %. However, as it has already been announced, the COP of the facility for α_{VGT} of 40 % was far from the optimum, and the efficiency of the turbine in the RBC did not reach the peak efficiency value reported by Serrano et al. [51] in a gas stand.

Based on these results, using a scaling tool for the modeled turbocharger is justified since the turbine and TCC performance showed them to be wrongly sized for the facility. The turbine is oversized, and the turbocharger compressor could be bigger to offer a higher efficiency. However, in this analysis, the scale factor available in VEMOD (other examples of applications can be found in [58,59]) will be applied only to the turbine since it is the most influential component for COP improvement [38].

The scale factor will be applied to the turbine based on its inlet conditions to operate at high-efficiency points across different speeds. This scaling maintains the similarity in the turbine by keeping non-dimensional groups constant. Non-dimensional mass flow and speed,
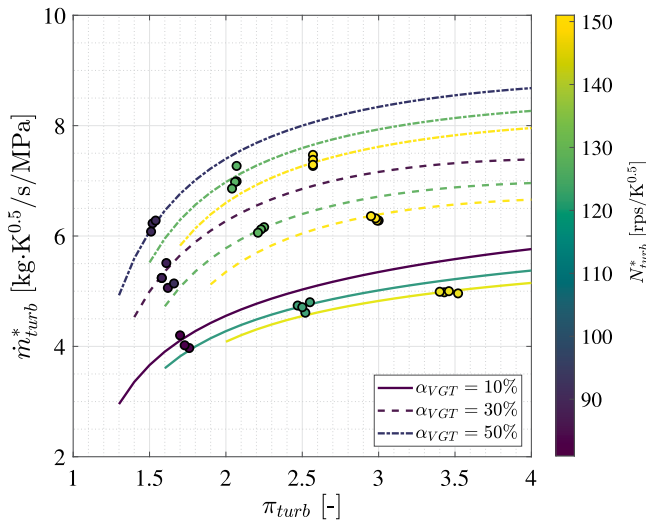
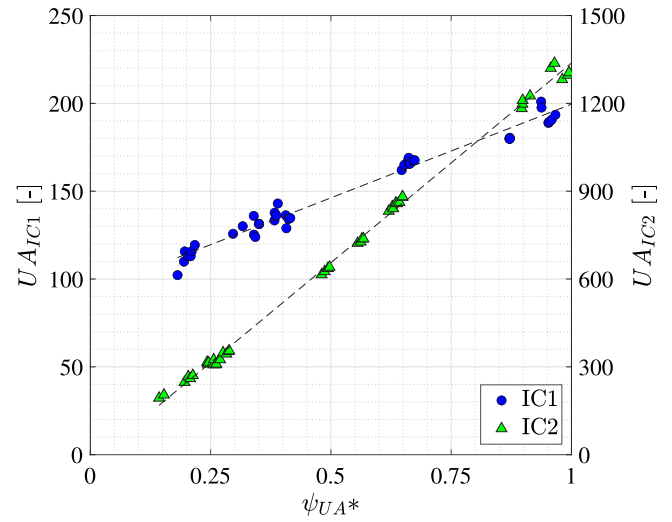**Fig. 10.** Turbine map built with experimental points from RBC testing facility.

Fig. 11. UA model correlation adjustment for both ICs using experimental data from testing campaigns.

calculated using Eqs. (3) and (4) are employed for this scaling:

$$\hat{m} = \frac{\dot{m}\sqrt{\gamma R T_{01}}}{D^2 p_{01} \gamma} \tag{3}$$

$$\Omega = \frac{N D}{\sqrt{\gamma R T_{01}}} \tag{4}$$

Adiabatic maps are generated to calculate efficiencies, which are assumed constant for all operating points. Actual efficiencies are then determined by calculating heat transmission and friction losses, which vary with geometric changes due to the scaling factor applied in each case.

The coolers were modeled using the experimental dataset from the RBC facility; water mass flow and inlet temperature and air mass flow and temperature at both the inlet and outlet in each cooler were employed to obtain the amount of energy heat transferred to the water. The exchanged heat in each intercooler, $\dot{Q}$, is defined by Eq. (5)

$$\dot{Q} = U \cdot A \cdot LMTD \tag{5}$$

Where U is the heat transfer coefficient, a measure of how the IC exchanges heat; A is the heat transfer exchange area, this is, the surface of tubes and fins used to exchange heat between air and water; and $LMTD$ is the logarithmic mean temperature difference, a measurement of the average temperature difference between the fluids involved in the heat exchange process. As U and A are internal parameters of the IC and U varies under different operating conditions, a new parameter is defined as UA (Eq. (6)), and it is obtained for each point of the experimental dataset.

$$UA = \frac{\dot{Q}}{LMTD} \tag{6}$$

After that, a correlation was built to link the UA value of each cooler to their operating conditions. Water flow rate, Q_w, Reynolds number, and the variation in temperature in the air side of the IC were chosen as the parameters to build the correlation. The expression is shown in Eq. (6):

$$\psi_{UA} = Q_w^a \cdot Re_{air,in}^b \cdot (T_{air,out} - T_{air,in})^c \tag{7}$$

Where a, b, and c are constant parameters adapted for each IC to optimize the expression adjustment to the experimental dataset through a linear regression. Results from the adjustment for IC1 and IC2 can be seen in Fig. 11. Each IC has its own axis to define its UA since the parameter achieves one order of magnitude more in the case of IC2 (because of the higher demand that suffers due to the two subsequent
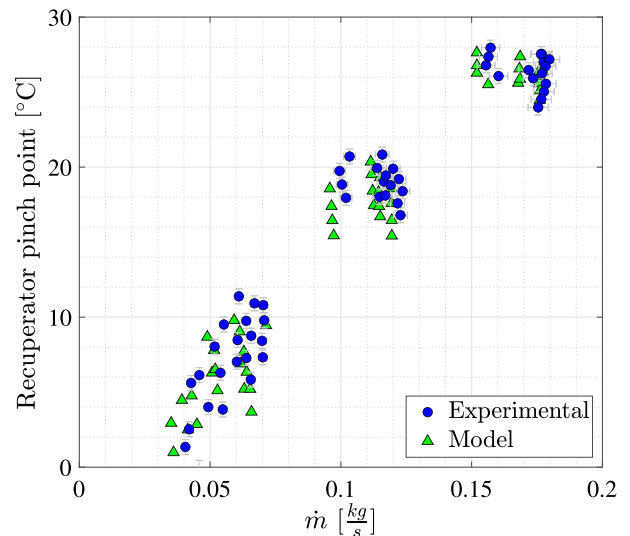

Fig. 12. Pinch point in the recuperator comparison between experimental and modeling data.

compression stages in EC2 and TCC before entering IC2). The x-axis of the plot has been normalized with the maximum value of ψ_{UA} obtained for each IC. This is the reason why values are contained between 0–1, calling this corrected parameter $\psi_{UA} *$. Both ICs responded well to the built correlation; the coefficient of determination, R^2, is over 0.98 for IC1 and 0.99 for IC2. Therefore, the results were added to the computational model.

The recuperator counted with an efficiency correlation provided by the manufacturer depending on the mass flow, which was introduced in the model. Pressure losses were characterized experimentally with pressure sensors placed at their inlet and outlet ducts. Results of the modeling of the recuperator can be seen in Fig. 12, showing how the model fits the experiment results with a maximum discrepancy of ±3 °C. Besides, the climatic chamber where the thermal resistance was placed was also characterized in terms of pressure losses, allowing the model to estimate the overall performance of the cycle based on the MFR through the facility.

With all of the present adjustments, a whole RBC model was built, permitting the attainment of results from different cycle configurations and saving time and money invested in the experimental test rig.
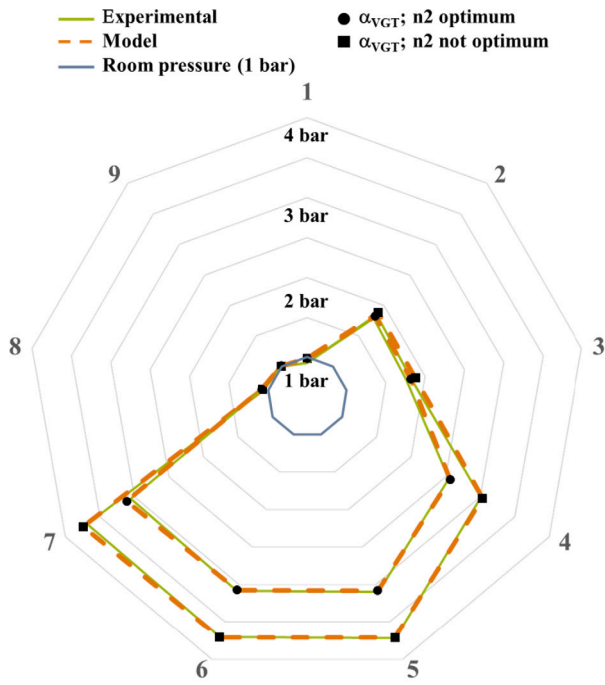
Fig. 13. Pressure evolution in the RBC. Model validation against experimental results.

Fig. 14. Temperature evolution in the RBC. Model validation against experimental results.

However, despite having modeled every element separately, they must replicate the cycle performance under different circumstances to show the model utility. To do so, two different RBC operating points are shown, with the target mentioned in the previous section (to cool 2 kW at −100 °C in the climatic chamber). A combination of α_{VGT} and n_2 that offered an optimum COP and another combination of these parameters that did not reach an optimum COP in the facility are shown in Figs. 13 and 14. In Fig. 13 the pressure evolution through stations 1–9 (numeration is done according to Fig. 2) is shown. Each polygon vertex represents one of those stations, corresponding with the places where thermocouples and pressure sensors were placed in the experimental facility. It is appreciated how the modeled cycle (dotted lines) replicates the experimental results with high accuracy for the two cases depicted. A slight overestimation in pressure can be observed between 6–7, meaning that the pressure loss in the recuperator is underestimated, with the maximum pressure differences recorded in a ±60 mbar range. Additionally, the affection of the control parameters to the cycle can be well observed since a lower π_{EC2} (p4/p3) is needed in the optimum case (circle dots) while π_{EC1} (p2/p1) remains mostly equal for both cases. A better choice in α_{VGT} reduces the needs in terms of pressure, and the ability to reduce π_{EC2} drives an increase of efficiency according to Fig. 8, enhancing the performance of the overall cycle.

In Fig. 14, the evolution in temperature through the whole cycle is depicted. Maximum differences of ±4 °C were found between experimental and model results, reported in this case after the compression stage in EC1 (T2/T1), meaning that if a good pressure agreement was obtained, the efficiency of this element should be improved in the model. Nonetheless, in every case, experimental and modeled, the target is sufficiently achieved, 173 K (−100 °C) at station 9. If in the experimental procedure section, it was explained that the test rig was equipped with a PID that controlled n_1, the same has been modeled in VEMOD, and a PID controller was varying the rotational speed of EC1 until convergence of target temperature was obtained at station 9. Since the temperature leap provoked by the expansion of the turbine is not quite big (below 30 °C), small inaccuracies in turbine efficiency are not a major issue, and the model will predict the experimental behavior. As it happened in the pressure analysis from Fig. 13, the maximum
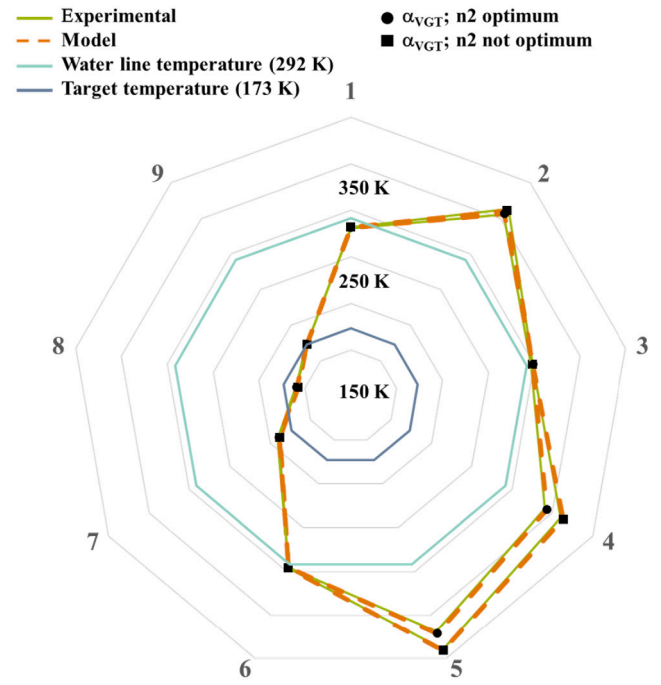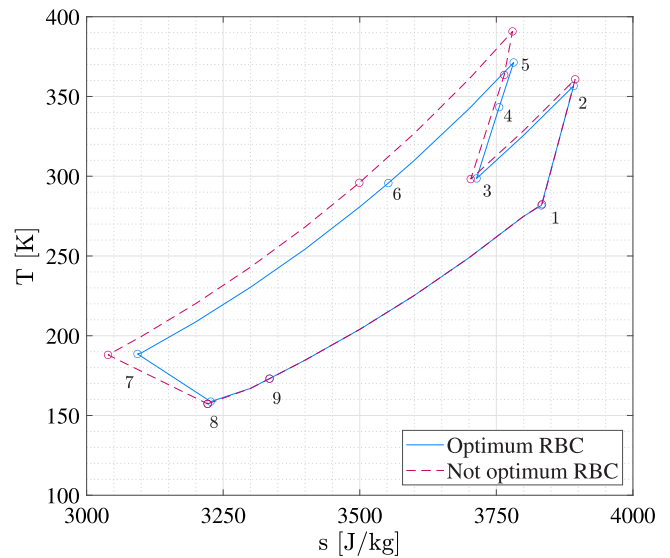

Fig. 15. Temperature vs entropy diagram in the RBC for two cases. Experimental results.

temperature achieved in the optimum case is lower than in the non-optimum. This is due to the lower demands in the overall pressure ratio since the compressors would not need to increase that much pressure and temperature. Once again, the agreement in obtained temperature for each element analyzed is good between experimental and modeled cases, and the model is shown to be operative and valid for analysis purposes.

To better understand the process, the two experimental cases shown in Figs. 13 and 14 were plotted in a temperature-entropy diagram, resulting in Fig. 15. It can be seen that the low-pressure side of the cycle (8-9-1) is equal mainly for the two cases since it is dependent on the boundary conditions. Once the expansion occurs in the turbine, pressure is fixed at ambient conditions since the climatic chamber
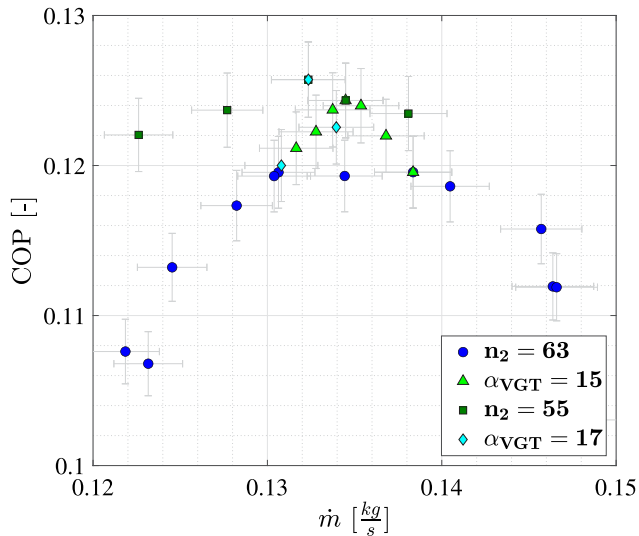
Fig. 16. COP vs MFR using the optimization technique proposed in Fig. 5 in the RBC facility. Experimental results dissipating $2\,\mathrm{kW}$ at $-100\,°\mathrm{C}$.

Fig. 17. Comparison of the evolution of COP and $\eta turb$ with MFR for different α_{VGT} at constant $n_2 = 63\%$. Experimental results dissipating $2\,\mathrm{kW}$ at $-100\,°\mathrm{C}$.

cannot stand pressure differences with its surroundings. Point 9 is asked to be at $-100\,°\mathrm{C}$, and point 1 is determined from the water line (Fig. 14) and the losses in the circuit (equivalent between cases because MFR is at the same order of magnitude). From that point, changes between cycles begin to be noticeable, and the optimum case requires less compression work in each of the three stages between point 1 and point 5. The compression stage segment corresponding to EC2 (3–4) is much shorter in the optimum case, reducing the work and increasing COP. Point 6 for each case has approximately the same temperature again due to the water line temperature. Finally, looking at the expansion segment (7–8), it is clear that the turbine efficiency is higher in the optimum case since it has a greater slope closer to the isentropic process.

5. Results discussion

Following the procedure from Fig. 5, an optimization process was done, showing experimental results in Fig. 16. A first try with $n_2 = 63\%$ was done for 10 different α_{VGT} positions. MFRs from $0.122\,\mathrm{kg\,s^{-1}}$ to $0.146\,\mathrm{kg\,s^{-1}}$ were covered just by changing the vanes of the turbine stator for each point. Meanwhile, n_2 was kept constant, and n_1 adjusted to meet the target temperature. A giant variation in COP can be seen in the dark blue circles since for the smaller MFR, the COP is slightly over 0.105, whereas in MFRs between $0.13\,\mathrm{kg\,s^{-1}}$ and $0.14\,\mathrm{kg\,s^{-1}}$ kg/s, the COP is rather constant at 0.12. Finding an optimum α_{VGT} for that $n_2 = 63\%$, COP can vary over 15%. Moreover, at this point, the procedure is similar to the one shown in Fig. 4, where the optimum COP was 0.105 at $0.133\,\mathrm{kg\,s^{-1}}$, and the range of optimum MFR is found to be the same in both cases, but offering a higher COP just by setting EC2 at a higher efficiency point. Once the boundaries of optimum α_{VGT} for a certain n_2 have been found, the next step of the process is to fix the position of α_{VGT}, and vary n_2. In this case, it is decided to start by decreasing this parameter, and soon, an improvement in COP will appear. This step is illustrated with light green triangles in Fig. 16. Without changing the angle of the turbine stator, it is checked how the range of MFR that can be covered is much smaller. Studied MFRs go from $0.130\,\mathrm{kg\,s^{-1}}$ to $0.138\,\mathrm{kg\,s^{-1}}$, and COP is increased up to 0.124 when $n_2 = 55\%$.

After the two steps were performed, partial optimums of both control parameters were found. However, they need to be double-checked since α_{VGT} was found optimum for the first try in n_2, but not for the second. Then, with $n_2 = 55\%$ a new swept of α_{VGT} was done. In this case (shown with dark green squares), a wider area of MFR
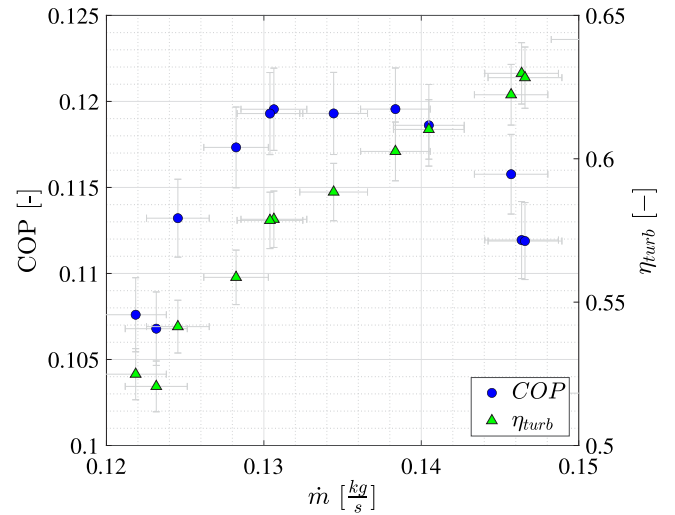
is covered with less impact on the COP, as it happened with the first step of this optimization procedure since α_{VGT} affects the MFR more. Values from $0.122\,\mathrm{kg\,s^{-1}}$ to $0.138\,\mathrm{kg\,s^{-1}}$ were checked, with the optimum being found at $0.133\,\mathrm{kg\,s^{-1}}$ where COP reached a value of 0.126 (it can be seen how the room for improvement is being reduced with every iteration, showing at the same time that the planned procedure works in the desired way). A new step of the optimization process is done, from the new optimum in α_{VGT}, new attempts of n_2 are completed. This time, light blue diamonds represent the variation of COP for n_2 over and below the aforementioned value of 55%. In both cases, COP decreases markedly, as it happened with the procedure step marked with triangles, indicating that COP is more sensible to changes when α_{VGT} is fixed (at a position that keeps MFR in the optimum range), and the efficiency of EC2 is changing with different n_2 values, finding $n_2 = 55\%$ combined with $\alpha_{\mathrm{VGT}} = 17\%$ to show the optimum performance.

Hence, with the available control parameters at the current facility, it can be ensured that the optimum COP for cooling $2\,\mathrm{kW}$ at $-100\,°\mathrm{C}$ is 0.126, with a power consumption of the facility of slightly over $15\,\mathrm{kW}$.

Once the optimum parameters have been experimentally found, it is certified that the chosen VGT is operating far from its optimum efficiency since the α_{VGT} that offered the best COP was around 20%. This effect can be visualized at Fig. 17 where the corresponding turbine efficiency is plotted for every tested point during the optimization process for $n_2 = 63\%$ (This one has been chosen since it counted with the broadest experimental dataset). The correlation between α_{VGT} and efficiency is mostly linear meanwhile at the lowest α_{VGT} position, with an MFR of 0.122, the efficiency of the turbine is around 0.52, at the maximum MFR measured, corresponding with the greatest α_{VGT} value, the efficiency increases over 0.62. However, that increase only positively influences COP until MFR reaches around $0.14\,\mathrm{kg\,s^{-1}}$. The weight of MFR in COP decreases overall performance from a specific value of MFR, no matter how much the turbine performance improves. This is due to the increase in compressor work necessary to move a higher MFR to accomplish the same demand in refrigeration terms.

Once a particular MFR has been shown as optimum to maximize COP for a certain application (fixed thermal load and fixed target temperature), it can be appreciated how the α_{VGT} necessary to reach that MFR differs from the one that offers the optimum turbine efficiency. Results from Serrano et al. [38] showed how the turbine is the key element when an increase in COP is sought. However, empirical results shown in this work show evidence that the whole system needs to be considered. The fact that the turbine vane position needs to be below its
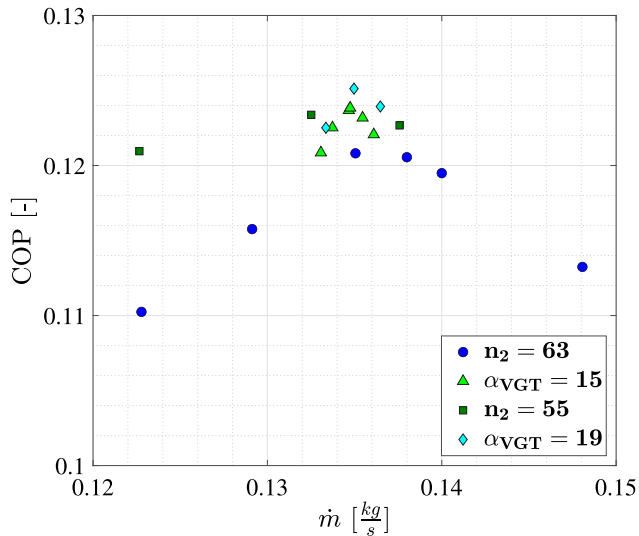
Fig. 18. COP vs MFR using the optimization technique proposed in Fig. 5 in the RBC facility. Model in VEMOD results.

Table 2
Model results from the scale of the turbine to show potential COP improvements with alternative turbine selection.

SF	COP	COP improvement [%]	η_T [%]	α_{VGT} [%]
1	0.125		62.4	19
0.967	0.131	4.8	64.8	20
0.933	0.142	13.7	66.5	23
0.9	0.144	14.9	67.0	26
0.867	0.147	17.1	68.1	29
0.833	0.137	9.7	66.7	30
0.8	0.121	−5.1	65.0	32

Table 3
Model results from the scale of the turbine to show potential compressor performances with alternative turbine selection.

SF	π_{EC1}	π_{EC2}	π_{TCC}	η_{EC1}	η_{EC2}	η_{TCC}
1	1.90	1.42	1.22	71.6%	76.7%	65.0%
0.967	1.87	1.40	1.22	72.0%	76.9%	66.1%
0.933	1.82	1.39	1.22	72.1%	76.7%	67.0%
0.9	1.80	1.39	1.23	72.1%	76.5%	68.5%
0.867	1.77	1.38	1.23	72.2%	76.0%	69.3%
0.833	1.76	1.39	1.25	72.2%	76.2%	73.2%
0.8	1.82	1.39	1.24	72.1%	76.1%	74.3%

optimum efficiency to maximize COP indicates that a smaller turbine would be desirable.

With the 1D model developed, a scaling of the turbocharger can be applied. Since the optimum MFR of the facility is known, a new control parameter is included in the model. Besides the target temperature (that controls n_1), α_{VGT} will be actuated by a PID controller in search of the optimum MFR. Before that, a complete simulation of the experimental optimization process shown in Fig. 16 is performed to check how close the model becomes to the experiment regarding COP. Overall results have already been shown in Figs. 13 and 14, with the optimum cycle corresponding with the optimum found in Fig. 16, and the non-optimum being one of the lowest COPs (MFR = $0.125\,\mathrm{kg\,s^{-1}}$ for $n_2 = 63\,\%$). The good agreement when looking at the general performance of the cycle in pressure and temperature (with variations of ± 60 mbar and $\pm 4\,^\circ$C) can show greater discrepancies when looking at a derived component as it is the COP, obtained as shown in Eq. (2).

Applying the optimization procedure sketched in Fig. 5 to the 1D model offered the COP vs MFR distribution that can be seen in Fig. 18. Comparing the obtained simulation results with those from Fig. 16 there can be seen how the experimental trend is followed, for the case of $n_2 = 63\,\%$ the bell-shaped distribution of COP through the MFR studied is replicated. Maximum COP values are slightly higher in the case of the simulation results (0.121 in comparison with 0.119 in the experiment). When α_{VGT} is fixed in the model, a narrowing in the range of MFR covered by the facility is noted. The model is less sensitive to MFR changes when n_1 and n_2 are being changed for a constant turbine position. Nonetheless, an increase in COP up to 0.124 matches the experimental results. When n_2 is fixed constant for a second time, another increase in COP is noted, but this time for a higher MFR (requiring a slightly higher α_{VGT} position) than that found optimum at the experiment. In this case, the optimum COP was reached at an MFR of $0.135\,\mathrm{kg\,s^{-1}}$, being this COP value of 0.125 quite similar to the 0.126 found experimentally within the error bar limits.

The analysis of results offered by the 1D model ensures that it is a valuable tool to replicate the experiments at the RBC test bench. Consequently, the aforementioned scaling factor is applied to the turbine, trying to match the high-efficiency area of the turbine with the MFR that offers the maximum COP. The chosen value for the optimum MFR is $0.135\,\mathrm{kg\,s^{-1}}$, as that is the one with the optimum COP in the simulation. Therefore, a PID acting on α_{VGT} will seek that MFR. Results from the parametric study performed are shown in Table 2.

A scale factor (SF) down to 0.8 was applied to the turbine. A potential COP improvement of over $17\,\%$ (COP increases up to 0.147) can be achieved with a reduction of the size of the turbine of a $13\,\%$ (scale factor 0.867). This increase results from the rise in turbine efficiency, from 0.62 to 0.68. The simulations were performed with a constant TCC size, keeping it the same as in the real RBC facility. As the MFR is constant for every studied case, and the speed of the turbine increases, a higher π_{TCC} can be observed, with a better compression process efficiency. This is even more beneficial for the COP since it reduces the need for compression ratio from both EC1 and EC2 in two ways: a better use of the expansion and a higher profit from turbine work to increase the pressure in the RBC. The reduction of compression ratio can be seen in Table 3 where EC1 (the compressor with the highest workload) reduces its compression ratio from 1.90 to 1.77 for the optimum SF case, while EC2 needs a compression ratio of 1.42 in the base case, while for an SF of the turbine of 0.867 the compression required is 1.38. In the case of both ECs, as the mass flow required in each simulation is the same as in the base case, the working points in the compressor maps are not too far from the original ones, and the efficiency area is mostly the same. Consequently, there are few changes in efficiency for both ECs, below $1\,\%$. The TCC remains mostly equal, changing just from 1.22 to 1.23 in terms of compression ratio. Still, its efficiency is much higher, moving from 0.65 to 0.69 thanks to the change in the rotational speed provoked by the turbine modification in size.

6. Conclusions

This work presents an experimental optimization process to improve the COP in a Reverse Brayton Cycle (RBC) with three-stage serial compression, using air as the working fluid. The cycle, built with automotive components, has zero ODP, zero GWP, and an A1 ASHRAE classification. Air is assessed for temperatures below $-40\,^\circ$C, whereas other natural refrigerants like carbon dioxide and ammonia face challenges due to phase changes. The optimization is performed at $-100\,^\circ$C, dissipating 2 kW, a common scenario for WBC. Key conclusions from the study include

The design should focus on aligning the peak efficiency of components with the optimal MFR range to achieve maximum COP, which corresponds to a certain overall pressure ratio. If the MFR exceeds this range to maintain the same pressure ratio, the compressors consume more power, resulting in a lower COP for the facility.

Each compression stage should be controlled separately to optimize the COP. By adjusting the speed ratio of each electric compressor, COP can increase by up to 19 % within the optimal MFR range.

The relationship between COP and turbine efficiency is linear to the optimal MFR. Beyond this point, even if turbine efficiency improves, COP decreases due to the excess power consumed by the electric compressors at higher MFR. Since the turbine significantly impacts COP, adjusting its size can enhance COP by 17 % over the current setup. Therefore, selecting the turbine size according to the optimal MFR is crucial for maximizing COP. Further gains might be possible with a lube-less bearing turbine.

Declaration of competing interest

The authors declare that they have no known competing financial interests or personal relationships that could have appeared to influence the work reported in this paper.

Data availability

Data will be made available on request.

Acknowledgments

References

[1] J.M. Calm, The next generation of refrigerants–historical review, considerations, and outlook, Int. J. Refrig. 31 (7) (2008) 1123–1133, http://dx.doi.org/10.1016/j.ijrefrig.2008.01.013.

[2] W. Carrier, R. Waterfill, Comparison of thermodynamic characteristics of various refrigerating fluids, Refrig. Eng. (1924).

[3] T. Midgley Jr., A.L. Henne, Organic fluorides as refrigerants, Ind. Eng. Chem. 22 (5) (1930) 542–545, http://dx.doi.org/10.1021/ie50245a031.

[4] UN, The montreal protocol on substances that deplete the ozone layer, 1987, United Nations Environment Programme, New York, NY, USA.

[5] WMO, Scientific Assessment of Ozone Depletion: 2006, Global Ozone Research and Monitoring Project - Report No. 50, 572pp., Geneva, 2007, World Meteorological Organization, 2006.

[6] P. Brohan, J.J. Kennedy, I. Harris, S.F. Tett, P.D. Jones, Uncertainty estimates in regional and global observed temperature changes: A new data set from 1850, J. Geophys. Res.: Atmos. 111 (D12) (2006) http://dx.doi.org/10.1029/2005JD006548.

[7] L.V. Alexander, Global observed long-term changes in temperature and precipitation extremes: A review of progress and limitations in IPCC assessments and beyond, Weather Clim. Extrem. 11 (2016) 4–16, http://dx.doi.org/10.1016/j.wace.2015.10.007.

[8] S. Yana Motta, P. Domanski, Low-GWP Refrigerants Status and Outlook, in: 48th IIR Informatory Note on Refrigeration Technologies, Oak Ridge National Lab.(ORNL), Oak Ridge, TN (United States), 2022.

[9] S. Riffat, C. Afonso, A. Oliveira, D. Reay, Natural refrigerants for refrigeration and air-conditioning systems, Appl. Therm. Eng. 17 (1) (1997) 33–42, http://dx.doi.org/10.1016/1359-4311(96)00030-0.

[10] N. Sanchuli, S. Dan, H. Bagheri, Ammonia application in cooling systems, in: Progresses in Ammonia: Science, Technology and Membranes, Elsevier, 2024, pp. 113–132, http://dx.doi.org/10.1016/B978-0-323-88501-0.00004-5.

[11] S. Zhang, Y. Liu, Y. Chen, T. Zheng, Z. Lan, R. Wen, X. Ma, Low-temperature ammonia absorption refrigeration system based on the temperature difference uniformity principle: Optimization analysis, Appl. Therm. Eng. 244 (2024) 122584, http://dx.doi.org/10.1016/j.applthermaleng.2024.122584.

[12] M. Karampour, S. Sawalha, State-of-the-art integrated CO2 refrigeration system for supermarkets: A comparative analysis, Int. J. Refrig. 86 (2018) 239–257, http://dx.doi.org/10.1016/j.ijrefrig.2017.11.006.

[13] E. Söylemez, K.N. Widell, C.H. Gabrielii, Y. Ladam, T. Lund, A. Hafner, Overview of the development and status of carbon dioxide (r-744) refrigeration systems onboard fishing vessels, Int. J. Refrig. 140 (2022) 198–212, http://dx.doi.org/10.1016/j.ijrefrig.2022.05.007.

[14] P. Bansal, A review–Status of CO2 as a low temperature refrigerant: Fundamentals and R&D opportunities, Appl. Therm. Eng. 41 (2012) 18–29, http://dx.doi.org/10.1016/j.applthermaleng.2011.12.006.

[15] B. Hu, D. Wu, R. Wang, Water vapor compression and its various applications, Renew. Sustain. Energy Rev. 98 (2018) 92–107, http://dx.doi.org/10.1016/j.rser.2018.08.050.

[16] A. Meroni, B. Zühlsdorf, B. Elmegaard, F. Haglind, Design of centrifugal compressors for heat pump systems, Appl. Energy 232 (2018) 139–156, http://dx.doi.org/10.1016/j.apenergy.2018.09.210.

[17] Y. Tian, J. Shen, C. Wang, Z. Xing, X. Wang, Modeling and performance study of a water-injected twin-screw water vapor compressor, Int. J. Refrig. 83 (2017) 75–87, http://dx.doi.org/10.1016/j.ijrefrig.2017.04.008.

[18] H. Zhang, Z. Zhang, L. Tong, J. Yang, L. Wang, X. Li, Y. Zhang, P. Xu, Z. Yu, J. Zhang, Experimental research and model optimization of a novel mechanical vapor compression evaporation system driven by Roots steam compressor, Int. J. Refrig. 150 (2023) 185–199, http://dx.doi.org/10.1016/j.ijrefrig.2023.01.014.

[19] Q. Li, J. Piechna, N. Müller, Design of a novel axial impeller as a part of counter-rotating axial compressor to compress water vapor as refrigerant, Appl. Energy 88 (9) (2011) 3156–3168, http://dx.doi.org/10.1016/j.apenergy.2011.02.024.

[20] M. Tahmasebzadehbaie, H. Sayyaadi, Optimal design of a two-stage refrigeration cycle for natural gas pre-cooling in a gas refinery considering the best allocation of refrigerant, Energy Convers. Manag. 210 (2020) 112743, http://dx.doi.org/10.1016/j.enconman.2020.112743.

[21] H. Kalantar-Neyestanaki, M. Mafi, A. Ashrafizadeh, A novel approach for operational optimization of multi-stage refrigeration cycles in gas refineries, Int. J. Refrig. 80 (2017) 169–181, http://dx.doi.org/10.1016/j.ijrefrig.2017.05.001.

[22] M.-G. He, X.-Z. Song, H. Liu, Y. Zhang, Application of natural refrigerant propane and propane/isobutane in large capacity chest freezer, Appl. Therm. Eng. 70 (1) (2014) 732–736, http://dx.doi.org/10.1016/j.applthermaleng.2014.05.097.

[23] P. Giménez-Prades, J. Navarro-Esbrí, C.-M. Udroiu, A. Mota-Babiloni, Influence of subcooling in R-449a supermarket refrigeration system and screening of refrigerant mixtures for its energetic and environmental improvement, Appl. Therm. Eng. 236 (2024) 121787, http://dx.doi.org/10.1016/j.applthermaleng.2023.121787.

[24] A. Lamb, Refrigerant Choices for the Future–Small Industrial Refrigeration Applications, Institute of Refrigeration, 2016.

[25] D. Coulomb, J.-L. Dupont, V. Morlet, The impact of the refrigeration sector on climate change-35. informatory note on refrigeration technologies, Int. J. Refrig. (2017).

[26] G. Cavalier, Cold chain certification. Proceedings of the 25th IIR international congress of refrigeration: Montreal, Canada, august 24-30, 2019, Int. Inst. Refrig. (2019) http://dx.doi.org/10.18462/iir.icr.2019.1836.

[27] Y. Qin, N. Li, H. Zhang, B. Liu, Energy and exergy analysis of a linde-hampson refrigeration system using R170, R41 and R1132a as low-GWP refrigerant blend components to replace R23, Energy 229 (2021) 120645, http://dx.doi.org/10.1016/j.energy.2021.120645.

[28] F. Capra, F. Magli, M. Gatti, Biomethane liquefaction: A systematic comparative analysis of refrigeration technologies, Appl. Therm. Eng. 158 (2019) 113815, http://dx.doi.org/10.1016/j.applthermaleng.2019.113815.

[29] C. Jin, H. Son, Y. Lim, Optimization and economic analysis of liquefaction processes for offshore units, Appl. Therm. Eng. 163 (2019) 114334, http://dx.doi.org/10.1016/j.applthermaleng.2019.114334.

[30] S.W. Spence, W.J. Doran, D.W. Artt, G. McCullough, Performance analysis of a feasible air-cycle refrigeration system for road transport, Int. J. Refrig. 28 (3) (2005) 381–388, http://dx.doi.org/10.1016/j.ijrefrig.2004.08.005.

[31] S. Engelking, H. Kruse, Development of air cycle technology for transport refrigeration, in: International Refrigeration and Air Conditioning Conference, 1996, URL https://docs.lib.purdue.edu/iracc/348/.

[32] A. Biglia, L. Comba, E. Fabrizio, P. Gay, A. Mannini, A. Mussinatto, D.R. Aimonino, Reversed brayton cycle for food freezing at very low temperatures: Energy performance and optimisation, Int. J. Refrig. 81 (2017) 82–95, http://dx.doi.org/10.1016/j.ijrefrig.2017.05.022.

[33] A. Vega-Bosch, V. Santamarina-Campos, P. Bosch-Roig, J.A. López-Carrillo, V. Dolz-Ruiz, M. Sánchez-Pons, Assessing the feasibility of removing graffiti from railway vehicles using ultra-freezing air projection, Appl. Sci. 14 (10) (2024) 4165, http://dx.doi.org/10.3390/app14104165.

[34] V.K. Patel, B.D. Raja, A comparative performance evaluation of the reversed brayton cycle operated heat pump based on thermo-ecological criteria through many and multi objective approaches, Energy Convers. Manag. 183 (2019) 252–265, http://dx.doi.org/10.1016/j.enconman.2018.12.109.

[35] H. Zhao, Y. Hou, Y. Zhu, L. Chen, S. Chen, Experimental study on the performance of an aircraft environmental control system, Appl. Therm. Eng. 29 (16) (2009) 3284–3288, http://dx.doi.org/10.1016/j.applthermaleng.2009.05.002.

[36] B. Dugue, J.-P. Bernard, R. Bouzigon, M. Nardi, W. Douzi, J. Feirreira, J. Guilpart, G. Lombardi, E. Miller, I. Tiemessen, Whole body cryotherapy / cryostimulation. 39th informatory note on refrigeration technologies, Int. J. Refrig. (2020) http://dx.doi.org/10.18462/iif.NItec39.09.2020.

[37] F.D. Legrand, B. Dugué, J. Costello, C. Bleakley, E. Miller, J.R. Broatch, G. Polidori, A. Lubkowska, J. Louis, G. Lombardi, et al., Evaluating safety risks of whole-body cryotherapy/cryostimulation (WBC): a scoping review from an international consortium, Eur. J. Med. Res. 28 (1) (2023) 387, http://dx.doi.org/10.1186/s40001-023-01385-z.

[38] J.R. Serrano, V. Dolz, A. Gómez-Vilanova, J.A. López-Carrillo, Advanced exergy analysis of a reverse brayton cycle using air as working fluid for cryogenic purposes, Int. J. Refrig. (2023) http://dx.doi.org/10.1016/j.ijrefrig.2023.12.002.

[39] A.K. Dhillon, P. Ghosh, Exergetic analysis of reverse brayton cryocooler with different turbine arrangements for HTS power cables, Cryogenics 115 (2021) 103262, http://dx.doi.org/10.1016/j.cryogenics.2021.103262.

[40] X. Yang, L. Chen, Z. Wang, S. Chen, Y. Hou, Study on the coupled characteristics of high-speed centrifugal compressor and turboexpander of a reverse Brayton air refrigerator, Int. J. Refrig. 147 (2023) 20–28, http://dx.doi.org/10.1016/j.ijrefrig.2022.11.022.

[41] J.R. Serrano, V. Dolz, A. Ponce-Mora, J.A. López-Carrillo, Experimental assessment of a reverse [brayton] cycle based on automotive turbochargers and E-chargers for cryogenic applications, J. Eng. Gas Turb. Power 145 (2) (2022) http://dx.doi.org/10.1115/1.4055580, 021029. arXiv:https://asmedigitalcollection.asme.org/gasturbinespower/article-pdf/145/2/021029/6960717/gtp_145_02_021029.pdf.

[42] J.-H. Hao, Q. Chen, Y.-C. Xu, A global optimization method for regenerative air refrigeration systems, Appl. Therm. Eng. 65 (1–2) (2014) 255–261, http://dx.doi.org/10.1016/j.applthermaleng.2014.01.021.

[43] Y. Xu, F. Chen, Q. Wang, X. Han, D. Li, G. Chen, A novel low-temperature absorption–compression cascade refrigeration system, Appl. Therm. Eng. 75 (2015) 504–512, http://dx.doi.org/10.1016/j.applthermaleng.2014.10.043.

[44] Z. Sun, Q. Wang, Z. Xie, S. Liu, D. Su, Q. Cui, Energy and exergy analysis of low GWP refrigerants in cascade refrigeration system, Energy 170 (2019) 1170–1180, http://dx.doi.org/10.1016/j.energy.2018.12.055.

[45] S. Song, Z. Zhang, X. Zhou, Q. Ju, L. Chen, S. Chen, Y. Hou, Analytical and experimental study on operating characteristics of a closed-cycle turbo-refrigerator for deep freezing, Appl. Therm. Eng. (2024) 123442, http://dx.doi.org/10.1016/j.applthermaleng.2024.123442.

[46] S.W. Spence, W.J. Doran, D.W. Artt, Design, construction and testing of an air-cycle refrigeration system for road transport, Int. J. Refrig. 27 (5) (2004) 503–510, http://dx.doi.org/10.1016/j.ijrefrig.2004.02.003.

[47] R. T.M., C15 technical data sheet, 2024, URL https://www.rotrex.com/wp-content/uploads/2022/01/Rotrex-Technical-Datasheet-C15-Rev6.0.pdf.

[48] C.C. António, C. Afonso, Air temperature fields inside refrigeration cabins: A comparison of results from CFD and ANN modelling, Appl. Therm. Eng. 31 (6–7) (2011) 1244–1251, http://dx.doi.org/10.1016/j.applthermaleng.2010.12.027.

[49] T. Lai, Y. Guo, Q. Zhao, Y. Wang, X. Zhang, Y. Hou, Numerical and experimental studies on stability of cryogenic turbo-expander with protuberant foil gas bearings, Cryogenics 96 (2018) 62–74, http://dx.doi.org/10.1016/j.cryogenics.2018.10.009.

[50] M.V. Zagarola, K.J. Cragin, J.A. McCormick, Operation of gas bearings at cryogenic temperatures, Cryogenics 105 (2020) 103001, http://dx.doi.org/10.1016/j.cryogenics.2019.103001.

[51] J.R. Serrano, L.M. García-Cuevas, V. Samala, J.A. López-Carrillo, H. Mai, Boosting the capabilities of gas stand data acquisition and control systems by using a digital twin based on a holistic turbocharger model, in: Internal Combustion Engine Division Fall Technical Conference, Vol. 85512, American Society of Mechanical Engineers, 2021, V001T07A002, http://dx.doi.org/10.1115/ICEF2021-66745.

[52] I. Iso, B. OIML, Evaluation of Measurement Data - Guide to the Expression of Uncertainty in Measurement, Geneva, Switzerland, 2008.

[53] P. Olmeda, A. Tiseira, V. Dolz, L. García-Cuevas, Uncertainties in power computations in a turbocharger test bench, Measurement 59 (2015) 363–371, http://dx.doi.org/10.1016/j.measurement.2014.09.055.

[54] G. Lombardi, E. Ziemann, G. Banfi, Whole-body cryotherapy in athletes: from therapy to stimulation. An updated review of the literature, Front. Physiol. 8 (2017) 258298, http://dx.doi.org/10.3389/fphys.2017.00258.

[55] J. Martin, F. Arnau, P. Piqueras, A. Auñon, Development of an Integrated Virtual Engine Model to Simulate New Standard Testing Cycles, Tech. Rep. 2018-01-1413, SAE Technical Paper, 2018, http://dx.doi.org/10.4271/2018-01-1413.

[56] J.R. Serrano, P. Olmeda, F.J. Arnau, M.A. Reyes-Belmonte, H. Tartoussi, A study on the internal convection in small turbochargers. Proposal of heat transfer convective coefficients, Appl. Therm. Eng. 89 (2015) 587–599, http://dx.doi.org/10.1016/j.applthermaleng.2015.06.053.

[57] J.R. Serrano, F.J. Arnau, L.M. García-Cuevas, A. Dombrovsky, H. Tartoussi, Development and validation of a radial turbine efficiency and mass flow model at design and off-design conditions, Energy Convers. Manag. 128 (2016) 281–293, http://dx.doi.org/10.1016/j.enconman.2016.09.032.

[58] J. Serrano, F. Arnau, L. García-Cuevas, V. Farias, Oxy-fuel combustion feasibility of compression ignition engines using oxygen separation membranes for enabling carbon dioxide capture, Energy Convers. Manag. 247 (2021) 114732, http://dx.doi.org/10.1016/j.enconman.2021.114732.

[59] J.R. Serrano, F.J. Arnau, L.M. García-Cuevas, F.A. Gutiérrez, Coupling an oxygen generation cycle with an oxy-fuel combustion spark ignition engine for zero NOx emissions and carbon capture: A feasibility study, Energy Convers. Manag. 284 (2023) 116973, http://dx.doi.org/10.1016/j.enconman.2023.116973.